Effect of engineered lattice contraction and expansion on the performance and CO_2 tolerance of $Ba_{0.5}Sr_{0.5}Co_{0.7}Fe_{0.3}O_{3-\delta}$ functional material for intermediate temperature solid oxide fuel cells

Idris Temitope Bello[a], Na Yu[a], Shuo Zhai[a,*], Yufei Song[b], Siyuan Zhao[a], Chun Cheng[a], Zhenbao Zhang[a], Meng Ni[a,*],

[a]Department of Building and Real Estate, Research Institute for Sustainable Urban Development (RISUD) & Research Institute for Smart Energy (RISE), The Hong Kong Polytechnic University, Hung Hom, Kowloon, Hong Kong, China

[b]Department of Mechanical and Aerospace Engineering, The Hong Kong University of Science and Technology, Clear Water Bay, Hong Kong, China

* Corresponding author: meng.ni@polyu.edu.hk (M. Ni);

zhaishuo.zhai@connect.polyu.hk

Abstract

Barium Strontium Cobalt Iron Oxide (BSCF) is a famous cathode material for solid oxide fuel cells (SOFCs) due to its excellent catalytic activity for oxygen reduction reaction (ORR) at intermediate and low operating temperatures. Its poor stability, however, in a CO_2-containing environment limits its practical application. In this study, we systematically investigate the effects of instigating lattice contraction and expansion on the performance and CO_2 tolerance of $Ba_{0.5}Sr_{0.5}Co_{0.7}Fe_{0.3}O_{3-\delta}$ (BSCF) air electrode functional material. We strategically substituted 5 mol.% Fe-B-site cations of BSCF with transition metals (TMs), i.e., Zn and Cu, to achieve lattice expansion and contraction, respectively. The $Ba_{0.5}Sr_{0.5}Co_{0.7}Fe_{0.25}Cu_{0.05}O_{3-\delta}$ (BSCFC5)

cathode, where lattice contraction occurred, exhibits the best performance with an area-specific resistance (ASR) of 0.0247 Ω cm^2 and a high peak power density (PPD) of 1715 mW cm^{-2} at 650 ℃ for the symmetrical and single cells, respectively. The functional material also exhibits enhanced tolerance to CO_2 compared to BSCF by surviving several rounds of 10% CO_2 injection and ejection for an overall nonstop testing period of 100 hours. The improved ORR, stability, and CO_2 tolerance instigated by lattice contraction in BSCF provides an insight into the adoption of this approach in achieving optimal desirable properties in SOFC cathode functional materials.

Keywords: Solid oxide fuel cells; cathode; lattice contraction and expansion; oxygen reduction reaction activity; CO_2 tolerance.

1.0 Introduction

The universal interest to ameliorate the increasing negative environmental impacts caused by fossil-based products has brought solid oxide fuel cells (SOFCs) to the limelight. Research has revealed that SOFCs are a viable solution to the achievement of a clean, safe, and highly efficient power source [1,2]. The current trend in the research for SOFCs is the development of low and intermediate temperatures (i.e., 350-700 ℃) SOFCs [3,4]. This is to enhance the service life, minimize material degradation and manufacturing costs, and fast-track the process of overcoming other challenges posed by SOFCs operating at high temperatures (i.e., 800-1000 ℃) [5]. The reduction of the operating temperature of SOFCs, however, significantly decreases the electrolyte conductivity and cathode catalytic activity causing an increase in the ohmic and polarization resistances of SOFCs [6,7]. The electrolyte ohmic loss can be reduced by fabricating thin-film electrolytes, however, the polarization loss at the cathode for oxygen reduction reaction

(ORR) still limits the SOFC performance at reduced temperatures [3]. It is, therefore, paramount to develop cathode materials that can function efficiently at low and intermediate temperatures.

Excellent cathode materials for intermediate to low temperature operating SOFCs are expected to exhibit mixed ionic and electronic conductivity (MIEC) so that the reaction zones for catalytic ORR can be extended from the traditional triple phase boundaries (TPB) to the entire surfaces of the cathode material [5]. Different categories of compounds, such as perovskite oxides, spinel oxides, Ruddlesden-Popper (RP) oxides, fluorite oxides, etc., have been proposed and developed as potential candidates to satisfy most or all the requirements of ideal cathode material. Perovskite oxide compounds of the form ABO_3 have been asserted to be the most promising candidates for intermediate and low-temperature SOFCs[8]. This is due to the possibility of modifying the A- and B- sites of these oxides in the form of doping by introducing strategic stoichiometric amounts of one or more elements into their A- or B- sites [9]. This could cause a change in their catalytic activities, CO_2 tolerance, and electronic structures. Strategic doping has been extensively applied to tailor the structural properties of innumerable perovskite oxide compounds in form of lattice expansion and contraction for different functional applications. This could help to achieve improved oxygen diffusion in cathode materials during operation, reduced materials thermal expansion coefficient (TEC), enhanced materials tolerance to CO_2, and increased physical and chemical stability of cathode materials, etc. [10–14].

One of the cathode materials for SOFCs which has garnered lots of attention in the past decades is BSCF [15,16]. This material was reported to operate within the temperature range of 500 to 700 ℃ with a PPD of 1.01 Wcm^{-2} and an ASR of 0.071 Ω cm^2 at 600 ℃ thereby exceeding the performance record ever achieved by any other cathode material before that time (i.e., 2004) [16]. Since then, it has often been used as the benchmark for assessing the performance of later

developed cathode materials for SOFCs. The major impediment, however, to the universal adoption of this material for commercial SOFC applications is its susceptibility to CO_2 poisoning in a realistic ambiance [17]. Researchers have therefore adopted different mechanisms and approaches to modify the parent BSCF to either improve its catalytic ORR at lower temperatures or enhance its stability and CO_2 tolerance [11,18–23]. No study, however, to the best of our knowledge, has reported the use of lattice engineering in the modification of the performance and CO_2 tolerance of BSCF.

An increasing number of studies have employed lattice engineering to influence the catalytic ORR, stability, and CO_2 tolerance of cathode materials [14,24,25]. Escudero-Escribano et al.[24] outlined the introduction of contraction mechanisms in the structural lattices of electrocatalysts to tailor their activity, stability, and reactivity. Cai et al. [25] described the use of lattice engineering for the tuning of material band structures to achieve materials with improved performance and other desirable properties. Sun et al. [14] modulated the charge density of active Cobalt atom in $LaCoO_3$ by introducing Ce ions into its lattice thereby causing a contraction in the lattice structure of the material. This contraction consequently caused an improvement in the performance of the $LaCoO_3$ by reducing the electron tunneling distance thereby optimizing the charge density distribution of the material.

TMs (i.e., Cu and Zn) are established dopants to optimize the properties of SOFC cathode materials [11,26]. For instance, the phase structure transition of $La_2Ni_{1-x}Cu_xO_4$ has been reported to be altered due to the introduction of Cu dopants [27]. Also, other interesting properties such as ORR and stability have been reported to be enhanced by co-doping Cu with other elements as in the case of Pr_2NiO_4 [28,29]. It has also been asserted that Cu dopants help to enhance the bulk oxygen diffusion and stability of cathode materials by reducing the TEC of the cathode thereby

improving the durability [30]. Zn dopant has also been used to modify the activity and stability of cathode materials [11,31,32]. The correlation of the activity and CO_2 tolerance of BSCF with lattice expansion and contraction, however, has not been specifically reported to the best of our knowledge.

In this study, we have systematically investigated the effects of engineering lattice expansion and contraction on the performance and CO_2 tolerance of the pristine BSCF air electrode functional material. We strategically substituted 5 mol.% Fe-B-site cations of BSCF with TMs, Zn and Cu, to achieve an expansion and contraction, respectively. We were able to show how lattice engineering is a significant descriptor in illustrating the variability in the catalytic ORR and CO_2 tolerance of BSCF functional air electrode material.

2.0 Material and methods

2.1 Powder preparation

$Ba_{0.5}Sr_{0.5}Co_{0.7}Fe_{0.3}O_{3-\delta}$ (BSCF), $Ba_{0.5}Sr_{0.5}Co_{0.7}Fe_{0.25}Cu_{0.05}O_{3-\delta}$ (BSCFC5), and $Ba_{0.5}Sr_{0.5}Co_{0.7}Fe_{0.25}Zn_{0.05}O_{3-\delta}$ (BSCFZ5), powders were synthesized by the EDTA-citric acid complexing sol-gel method. Stoichiometric amounts of the following chemical reagents from Sinopharm: $Ba(NO_3)_2$, $Sr(NO_3)_2$, $Co(NO_3)_2.6H_2O$, $Fe(NO_3)_3.9H_2O$, $Cu(NO_3)_2.3H_20$, and $Zn(NO_3)_2.6H_2O$ were used to synthesize BSCF, BSCFC5, and BSCFZ5, respectively. At first, under a continuous stirring and heating condition, a homogeneous solution was formed by dissolving stoichiometric amounts of the chemical reagents in deionized water. Thereafter, the complexing agents; $C_{10}H_{16}N_2O_8$ (EDTA) and $C_6H_8O_7.H_2O$ (citric acid) were added to the solution under the same condition. The pH of the solution was then adjusted using NH_4OH (Ammonium hydroxide) until a slightly basic pH is achieved. The stirring and heating condition

was maintained until a gel-like fluid is formed. The gel was then heated in an aerated oven at a temperature of 180 ℃, for at least 8 h, until a black solid precursor is formed. The resulting precursors were then calcined at 1000 ℃ for 5h to generate BSCF, BSCFC5, and BSCFZ5.

2.2 Cell fabrication

2.2.1 Symmetric cells

To fabricate each of the following cells: BSCF │SDC │BSCF, BSCFC5 │SDC │BSCFC5, and BSCFZ5 │SDC │BSCFZ5, SDC powder (supplied by Fuel cell materials) was weighed at every instance and then pressed uniaxially to achieve a dense round pellet. The resulting pellets were then sintered at 1300 ℃ for 12 h. Thereafter, the powders of BSCF, BSCFC5, and BSCFZ5 were mixed with ethylene glycol, isopropyl alcohol, and glycerol to form a colloidal suspension by ball milling the mixture using Fritsch Pulverisette 6 at 400 rpm for 30 minutes. With the aid of a compressor pump and spray gun, the resulting colloidal suspensions were then sprayed uniformly on both sides of the dense SDC electrolytes. This was followed by sintering at a temperature of 850 ℃ for 2 h to form symmetric cells comprising porous electrodes (i.e., with a thickness of about 17 µm and an area of 0.5 cm^2) and electrolyte. Afterward, Ag paste was uniformly brushed on both sides of the cell to serve as the current collector and Ag wires were attached for taking electrochemical measurements.

2.2.2 Anode-supported single cells

The anode supported single cells with the configurations NiO-SDC │SDC │BSCF, NiO-SDC │SDC │BSCFC5, and NiO-SDC │SDC │BSCFZ5 were fabricated through the process of dry pressing and co-sintering. At first, the NiO-SDC cermet was produced by ball milling NiO, SDC, and starch powders in the ratio of 6.5:3.5:0.8 in pure ethanol for 1 h. Thereafter, the

resulting mixture was dried completely in the oven and then pressed into discs at a pressure of 100 MPa. This was followed by the addition and co-pressing of pure SDC electrolyte powders uniformly distributed across the cermet at a pressure of 200 MPa to achieve a dense electrolyte in the single cell. The co-pressed pellets were then sintered in the furnace at a temperature of 1300 ℃ for 5 h. In the end, the cathode slurry was sprayed on the SDC electrolyte like the approach described in Section 2.2.1, followed by sintering at a temperature of 850 ℃ for 2h to achieve a single cell. The resulting thickness of the cathode, electrolyte, and anode layers for the various cells was an average of ~10 µm, ~20 µm, and ~430 µm, respectively as illustrated in **Figure S2a.**

2.3 Materials characterization

The phase purity and crystal structure of the synthesized powders were investigated using x-ray diffraction (XRD, Rigaku SmartLab 9kW). The diffraction patterns were collected through a stepwise scanning process (i.e., 0.02^o step size) over the range of 20 – 80^o. Rietveld refinement of the XRD patterns for BSCF, BSCFC5, and BSCFZ5 was further carried out using FullProf Suite to get more detailed information about the crystal structures. Scanning electron microscopy (SEM) (TESCAN VEGA3) was used to investigate the morphology of the material at an accelerating potential of 20 kV. High-resolution transmission electron microscopy, HR-TEM, FEI Tecnai G2 F20 was also used to characterize the microstructure of the calcined BSCFC5 powder. The powders of BSCF, BSCFC5, BSCFZ5 which were calcined at 1000 ℃ for 5 h were dry pressed at a pressure of 200 MPa into a rectangular shaped block of dimensions $\sim 20\ mm \times 5\ mm \times 2\ mm$ followed by sintering at 1050 ℃ for 5 h. Thereafter, the electrical conductivities of the samples were measured in the temperature range of 300 ℃ to 800 ℃ using the four-probe DC configuration with Keithley 2440 source meter at a temperature interval of 10 ℃ [21].

Solarton 1260 frequency response analyzer and Solarton 1287 potentiostat were used to measure the polarization resistances of the symmetric cell samples at a temperature range of 500 ℃ to 700 ℃ in air. The measurements were performed under an open circuit condition with zero applied direct current potential and a 10 mV applied alternating current amplitude under a frequency range of 10 kHz to 0.1Hz. Thereafter, the performance of single button cells based on the cathode materials considered was assessed using *I-V-P* polarization tests in the temperature range of 500 ℃ to 650 ℃ using a four-probe configuration with Keithley 2440 source meter. The anode side of the single cells was fed with H_2 at a constant flow rate of 100 mL/min while the cathode side was exposed to ambient air.

3.0 Results and discussion

In perovskites, varieties of physicochemical properties related to their electrocatalytic behavior can be extracted from their crystal structure. **Figure 1a** illustrates the X-ray diffraction (XRD) profiles of BSCF, BSCFC5, and BSCFZ5 powders after undergoing calcination at 1000 ℃ for 5h. The profiles show that the perovskite structures of the powders are all single-phase with unique characteristic peaks. This confirms the successful doping of Zn and Cu into the perovskite lattice of BSCF to yield BSCFZ5 and BSCFC5, respectively. It can be observed from **Figure 1b** that the XRD pattern of BSCFZ5 shifted to a lower 2θ angle while that of BSCFC5 shifted to a higher 2θ angle. This confirms that the TMs doped into the Fe-B-site of BSCF led to an expansion and contraction in the unit cell volume. This suggests that the shrinkage and expansion in lattice cell volume could be due to the ionic radius of the substituted B-site element, Fe (Fe^{3+} = 0.645 nm, coordination = VI), relative to the introduced dopants, Zn (Zn^{2+} = 0.74 nm, coordination = VI) and Cu (Cu^{3+} = 0.54 nm, coordination = VI). In addition, the slight disparity in the crystal structures of both doped samples (BSCFC5 and BSCFZ5) could be attributed to the

difference in the electronic structures of the dopant elements (Cu and Zn) relative to the main B-site element, Co [33–35]. **Figure 1c** illustrates the crystal structural diagram of an idealized cubic BSCFC5 perovskite oxide with its A-site cation being in 12 coordination with O^{2-} and its B-site cation being in six coordination with O^{2-}. **Figure 1 (d-f)** present the XRD refinement patterns for BSCF, BSCFC5, and BSCFZ5, respectively. The samples all have symmetric cubic structures with the same space group ($Pm\bar{3}m$), but different lattice constants as expressed in **Table 1**. These values are consistent with those of earlier reported BSCF-based perovskite materials [21,36].

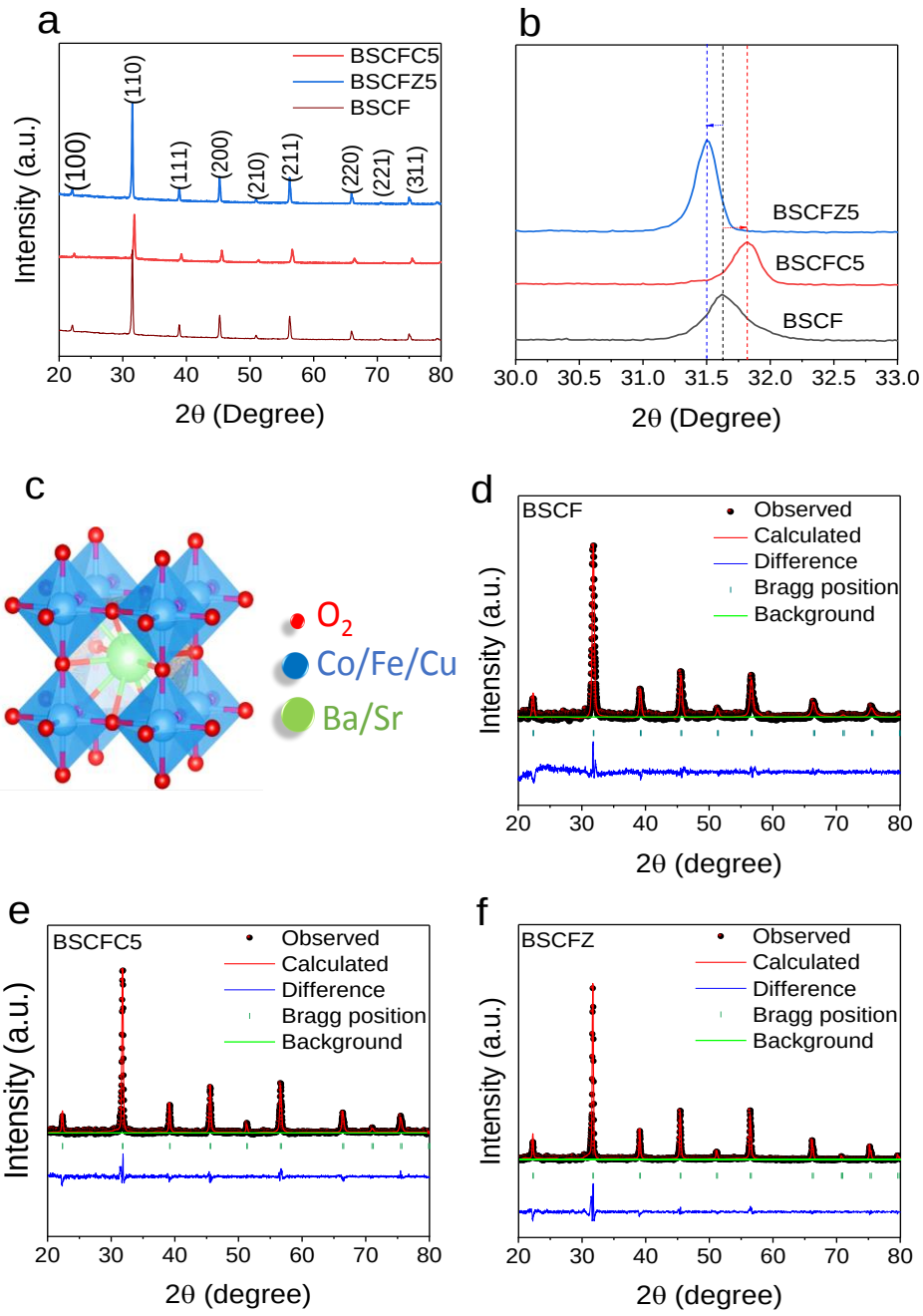

Figure 1: XRD patterns illustrating (a) the crystal structures for as-synthesized BSCF, BSCFC5, and BSCFZ5 powders (b) the magnified profile of the (110) plane of all the as-synthesized powders (c) cubic crystal structures of all the samples. Rietveld refinement for (d) BSCF (e) BSCFC5 (f) BSCFZ5.

Table 1 presents the lattice parameters, lattice volume, weighted profile reliability factor (Rwp), integrated intensity reliability factor (Rp), and goodness of fit (χ^2) for BSCF, BSCFC5 and BSCFZ5. There is a good agreement between the observed pattern and the calculated profile as illustrated in the data in **Table 1** which establishes the reliability of the refinement structural model. There is an observed contraction and expansion in the lattice volume of BSCF when its Fe-B-site cation is partially substituted with 5 mol.% of Cu and Zn, respectively. This can be confirmed from the shifting of the diffraction peaks of BSCF to a higher and lower diffraction angle when doped with Cu and Zn, respectively as illustrated in **Figure 1a**. This phenomenon is corroborated with the results from the Rietveld calculations presented in **Figure 1(d-f)** and **Table 1**.

Table 1: Refined lattice parameters for all the samples

Sample	a (Å)	b (Å)	c (Å)	V (Å)	wR_p (%)	R_p (%)	χ^2
BSCFC5	3.97944	3.97944	3.97944	63.02	8.44	6.87	1.72
BSCF	3.98116	3.98116	3.98116	63.10	6.18	4.44	1.49
BSCFCZ5	3.99232	3.99232	3.99232	63.63	4.59	6.38	1.61

To gain more insights into the influence of the dopants on BSCF in terms of the observed lattice shrinkage and expansion as well as their cationic oxidations states, X-ray photoelectron spectroscopy (XPS) was employed to characterize the surface elemental distribution and composition of BSCF, BSCFC5, and BSCFZ5. **Figure 2** illustrates the deconvoluted XPS profiles for Co2p, Fe2p, O1s, Cu2p and Zn2p for BSCF, BSCFC5, and BSCFZ5. XPS core-level spectra of a TM inadvertently provide useful insights into the valence state and electronic

structure of the TM ion. Hence, **Figure 2a** illustrates the spin-orbital splitting of Co $2p_{1/2}$ and Co $2p_{3/2}$ spectra which were deconvoluted using standard Gaussian-Lorentz. These resulting subpeaks could be designated as Co^{3+} and Co^{4+} as shown in **Figure 2a**. The binding energy values are in the range of ~792.97 eV – 795.82 eV at $2p_{1/2}$ and ~777.39 – 779.69 eV at $2p_{3/2,}$ which are consistent with past studies [12,37]. The spin-orbital splitting of Co 2p doublets is congruous with less than ~10 eV binding energy as detailed in **Table S2**. There are also no significantly identifiable satellite peaks in the binding energy range of ~785 – 790 eV suggesting the absence of Co^{2+} in all the samples[12]. **Figure 2b** presents the XPS spectra of Fe $2p_{3/2}$ in BSCF, BSCFC5, and BSCFZ5 and specific details can be found in **Table S3**. The spin-orbital splitting of Fe 2p electron spectra was fitted into subpeaks corresponding to the valence states Fe^{3+} (708.05 – 709.26 eV) and Fe^{4+} (710.53 – 712.37 eV), respectively. These results conform with existing reports [38,39]. The binding energy values of Co 2p and Fe 2p in BSCFC5 advanced in the higher energy direction while those of BSCFZ5 retreat towards the low energy direction suggesting the existence of expansion and contraction in the lattice volume of the engineered BSCF samples. The higher binding energy advancement could shorten the pathway for oxygen transport thereby enhancing the catalytic performance of BSCF, while the retreat towards the lower energy direction could lengthen the distance for oxygen transport and affect the ORR of BSCF[14,40]. **Figure 2c** shows the deconvolution of the O 1s spectra of all the samples considered into two characteristic subpeaks namely: the adsorbed oxygen (OH^-, CO_3^{2-}, O^{2-}, and O^-~531 eV) and the lattice oxygen (O^{2-}, ~529 eV) [36,41]. The peak positions and estimated percentages of the surface oxygen for BSCF, BSCFC5, and BSCFZ5 depicted in **Figure 2c** are presented in **Table 2.** The surface oxygen in all the specimens transforms in the order outlined in Eq. 1.

$$O_2 \leftrightarrow O_2 \xrightarrow{+e^-} O_2^- \xrightarrow{+e^-} O_2^{2-} \leftrightarrow 2O^- \xrightarrow{+2e^-} 2O^{2-} \quad (1)$$

Table 2: Percentages of adsorbed and lattice oxygen for BSCF and BSCFC5

Sample	Adsorbed oxygen		Lattice oxygen		Ratio
	Peak position (eV)	Percentage (%)	Peak position (eV)	Percentage (%)	O_{ads}/O_{lat}
BSCF	530.92	81.36	528.82	18.64	4.36
BSCFC5	531.90	83.28	529.66	16.72	4.98
BSCFZ5	530.16	67.67	528.94	32.33	2.09

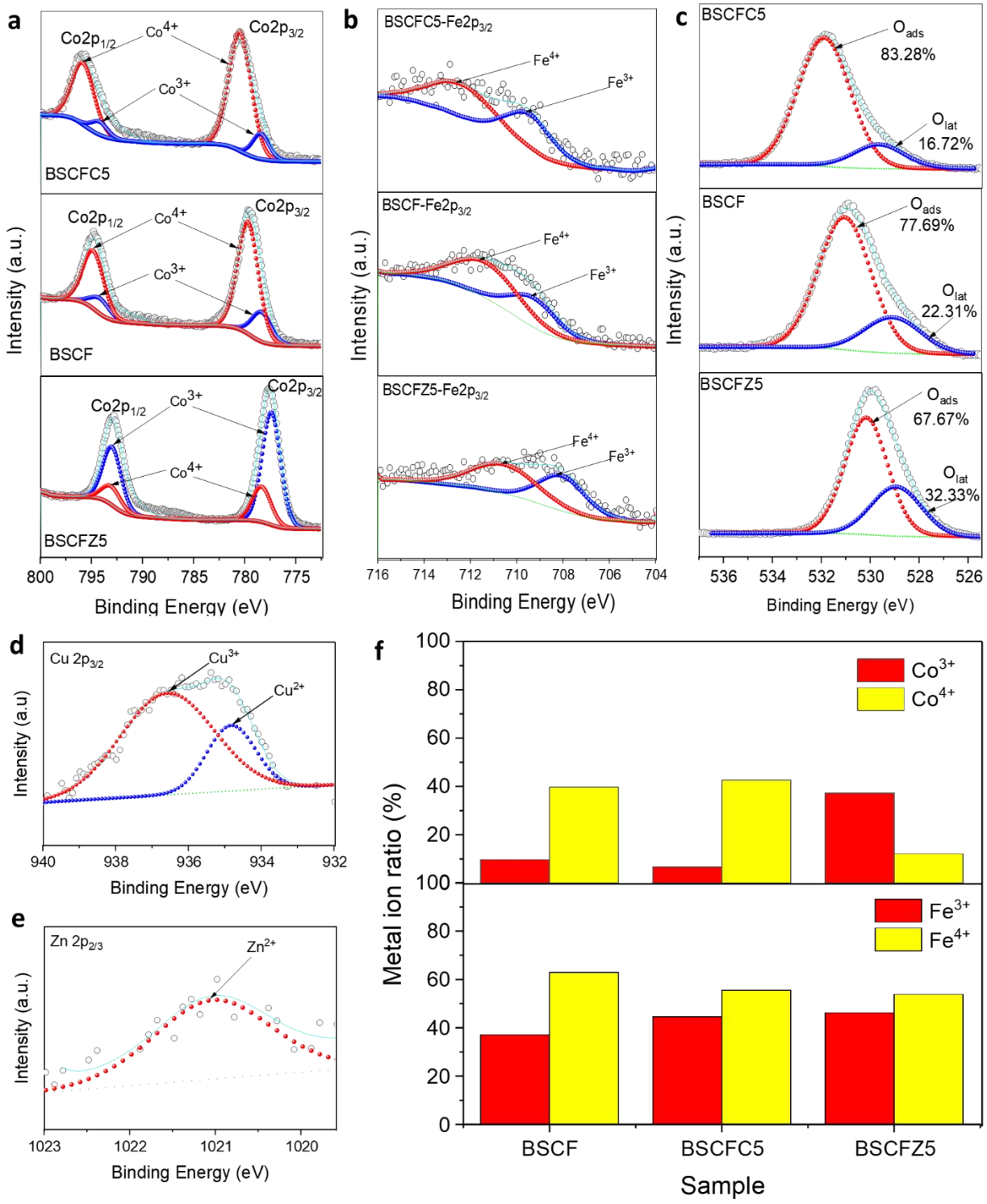

Figure 2**:** XPS spectra of the B-site elements of BSCF, BSCFC5, and BSCFZ5 (a) Co 2p (b) Fe 2p (c) O 1s. XPS spectra for (d) Cu 2p and (e) Zn 2p. (f) Percentage contribution of dominant B-site cations (a) $Co^{3+/4+}$ (b) $Fe^{3+/4+}$.

It can be observed from **Figure 2c** that the adsorbed oxygen for BSCFC5 is relatively higher than those of BSCF and BSCFZ5. This is because of the compressive strain on the lattice structure of BSCFC5; therefore, the relative volume of the adsorbates is increased and the pathway for oxygen diffusion in the lattice is shortened which will subsequently promote enhanced catalytic ORR. On the contrary, the smaller percentages of the adsorbed oxygen in BSCF and BSCFZ5 could be attributed to their relatively larger lattice volume since the pathway for oxygen diffusion will be extended. This phenomenon hints that the electrocatalytic performance of BSCFC5 could be better than those of BSCF and BSCFZ5 because of its higher O_{ads}/O_{lat} ratio which has been established in previous studies to influence ORR of cathode materials (i.e., the higher the ratio, the better the ORR)[42,43]. In the case of the Cu element depicted in **Figure 2d**, the Cu $2p_{3/2}$ spectra were deconvoluted into two peaks corresponding to Cu^{2+} and Cu^{3+} with binding energy values of ~934.69 eV and ~936.62 eV, respectively [44]. The Zn $2p_{3/2}$ spectrum from BSCFZ5 has a single peak which could be designated as Zn^{2+} (~1021 eV) as depicted in **Figure 2e** [45]. The intensities of Co^{3+}/Co^{4+} and Fe^{3+}/Fe^{4+} were calculated from the XPS analysis as illustrated in **Figure 2f.** It can be inferred that there is more electroneutrality in BSCFC5 with its B-site cations having a +3/+4 charge (i.e., $[CoFeCu]^{+3/+4}$. This explains the reason for the contraction in the lattice of BSCFC5 because the ionic radius of Cu^{3+} (0.54 nm, coordination = VI) relative to the other B-site elements with +3 charge (Co^{3+} = 0.61 nm, coordination = VI and Fe^{3+} = 0.645 nm, coordination = VI) is lower [46]. This will inadvertently instigate contraction in its lattice. On the other hand, the ionic radius of Zn^{2+} (0.74 nm) is larger than all other B-site cations in BSCFZ5 thereby engendering expansion in its lattice.

The electrical conductivities of BSCF, BSCFC5, and BSCFZ5 with respect to varying temperatures, measured in pure air, are presented in **Figure 3**a. The obtained conductivity values (i.e., BSCF) reasonably conform with those reported in previous studies [47,48].

The substitution of Fe-B-site cation of BSCF with Cu leads to the formation of negatively charged defects which requires compensation by positively point charge defects in the form of either holes or oxide ions, as expressed in the mechanistic expression in Eq. 2, to achieve a state of equilibrium.

$$CuO \xrightarrow{BSCF} (Cu_{Fe}^{2+})'' + 2\dot{h} + \frac{1}{2}O_2 \qquad (2)$$

The resulting balance in Eq. 2 contributes to the redox equilibrium involving the Co and Fe species as expressed in Eq. 3.

$$Cu_{Fe}^{2+} \rightarrow (Cu_{Co}^{3+})' + 2\dot{h} \qquad (3)$$

However, the estimation of the conductivity of an MIEC material such as BSCF and its derivatives (BSCFC5 and BSCFZ5) using direct current measurements, as in this case, generates combined electronic and ionic conductivities which coincide with holes and oxide ion migration, respectively. The intensity of this phenomenon, however, is dependent on the temperature variation as expressed in the defect's equilibrium expressions in Eq. 2 and 3. Therefore, from **Figure 3**a, it can be inferred that at low temperatures, below the transition point (i.e., around 450-500 ℃), the nature of conductivity is predominantly electronic and above the transition point, the progressive increase of ionic behavior is prevalent as expressed in the mechanistic expression in Eq. 3.

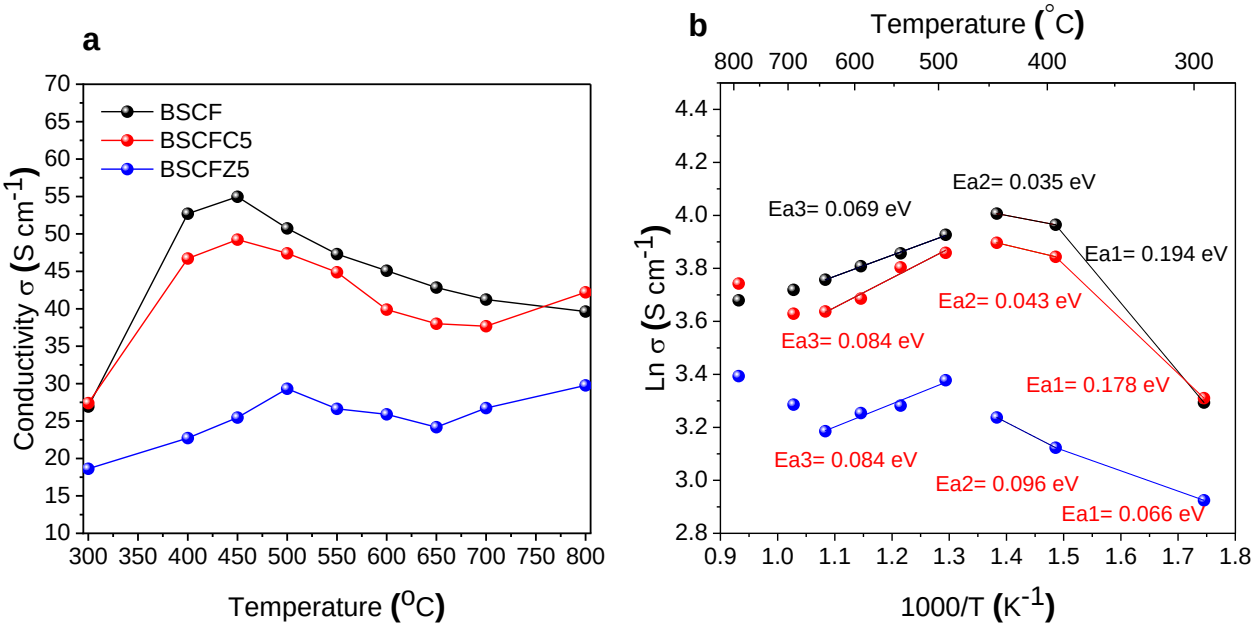

Figure 3: Dependence of electrical conductivity on temperature (a) conductivity of all the samples with respect to temperature (b) Arrhenius plots based on the electrical conductivity of the samples.

It can also be inferred from Arrhenius plots in **Figure 3**b that the order of decreasing conductivity in the samples studied can be summarized as BSCF>BSCFC5>BSCFZ5, implying that doping of BSCF did not enhance its electrical conductivity. This is because the substitution of Zn and Cu into the B-site of BSCF led to the reduction of Fe^{4+} and Co^{4+} to Fe^{3+} and Co^{3+}, respectively, thereby instigating the reduction in the charge carrier concentrations of BSCFZ5 and BSCFC5. This consequently engenders a decrease in the electrical conductivities of BSCFZ5 and BSCFC5 relative to BSCF. The conductivity behavior in the materials under consideration is non-uniform, hence the activation energies were estimated at several temperature ranges and the cumulative activation energies were summarized in **Table S4**. These activation energies were estimated using the expression $\sigma = \sigma_o e^{\frac{-Ea}{kT}}$, where Ea is activation energy and k is Boltzmann constant, T is the absolute temperature and σ_o is the pre-exponential factor. It can be observed

that the BSCF has the least activation energy in the intermediate temperature range of (500 – 650 ℃), followed by BSCFC5. However, in the low-temperature range of 300 – 400 ℃, BSCFZ5 has the least activation energy (i.e., 0.084 eV) which makes it eventually possess the smallest cumulative activation energy as depicted in **Table S4.**

Figure S1 presents the morphology of the BSCFC5 comprising the cross-section of the single cell. In **Figure S1a**, the SEM image of the single cell of BSCFC5 shows the layers of the anode, electrolyte, and cathode with their dimensions. The different layers are fused without any apparent significant debonding. It can also be observed that the anode and cathode are reasonably porous enhancing gas diffusion, and the electrolyte is well compacted to allow strictly for the migration of the oxygen ionic species. **Figure 4a** shows the Scanning transmission electron microscopy image (STEM) of BSCFC5. **Figure 4b** confirms that the distribution of all the elements, within the single grain, in the observed STEM image on the scale of 100 nm from **Figure 4a** are homogenous. The Energy dispersive spectroscopy (EDS) mapping in **Figure 4c** confirms that all the elements intended to be in BSCFC5 are present. The atomic percentages of the constitutive elements in BSCFC5 are also consistent with the stoichiometric proportion of the as-synthesized perovskite powder described in the materials synthesis section. The d-spacing for the BSCFC5 from the HR-TEM image was estimated to be 0.288 nm, corresponding to the plane (110), as illustrated in **Figure 4d.**

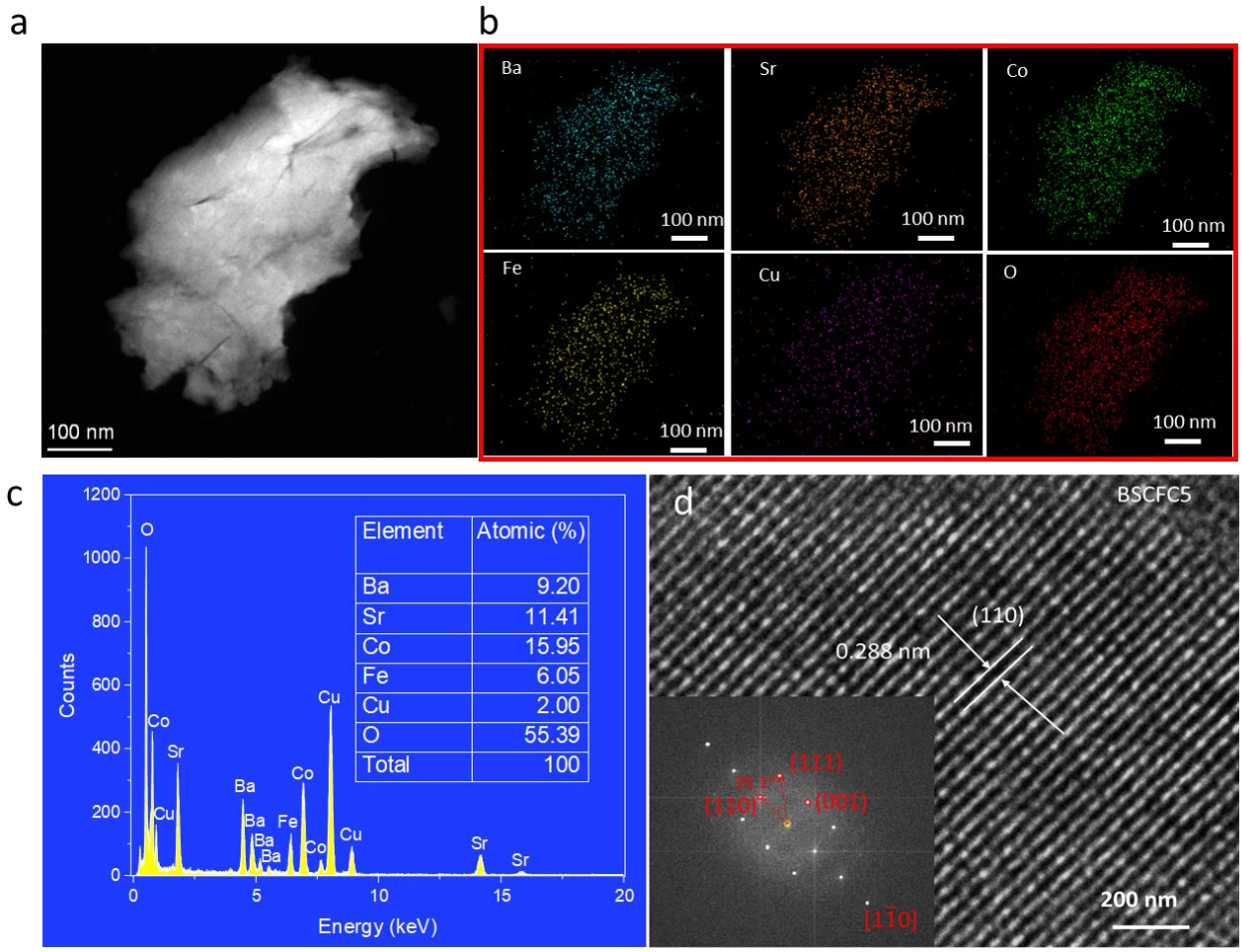

Figure 4**:** Schematics showing: (a) STEM of BSCFC5 (b) the energy-dispersive X-ray (EDX) of the constitutive elements in BSCFC5 (c) EDS mapping of the constitutive elements in BSCFC5 and their atomic percentages (d) the HR-TEM image of the BSCFC5.

The electrochemical performances of BSCF, BSCFC5, and BSCFZ5 cathode materials were evaluated using symmetric cells with SDC as the electrolyte in each case. The characterization of performances of the cathode materials was achieved by taking electrochemical impedance spectroscopy (EIS) measurements. **Figure 5a** presents the Nyquist plots of the EIS data measured at 600 ℃ for all the cathode materials considered. The difference between data points corresponding to high- and low-frequency values intercepting the horizontal axis of the Nyquist plot represents the area-specific resistance as illustrated in **Figure 5b**. Based on this, the ASRs

for the BSCF, BSCFC5 and BSCFZ5 at 600 ℃ are 0.081 Ω cm^2, 0.054 Ω cm^2 and 0.278 Ω cm^2, respectively. BSCFC5 exhibits the least ASR, followed by BSCF, and then BSCFZ5. The equivalent circuit model, R_{Ω}-(R_{E1}/CP_{E1})-(R_{E2}/CP_{E2}), was used to fit the EIS results of all the samples. The high-frequency polarization resistance can be attributed to the charge transfer process of oxygen ions at the interface between the electrode and the electrolyte while the low-frequency polarization resistance values can be associated with the oxygen adsorption-dissociation process in the cathode electrode [49]. The ASRs of the cathode electrode materials from 700 ℃ to 500 ℃ are summarized in **Figure 5d**. The BSCFC5 material exhibited the lowest ASR values (relative to the other materials) at all temperatures indicating that it has the best electrocatalytic ORR instigated by the contraction in its lattice structure. This suggests that lattice contraction could foster an improved performance of cathode materials as opposed to the supposition that lattice expansion alone promotes improved ORR. This is because the substitution of the Fe-B-site cation of BSCF with 5 mol.% Cu causes a reduction in the oxidation states of Co and Fe. This consequently shortens the pathway for oxygen diffusion thereby accelerating the catalytic ORR kinetics. Also, it could be due to the weakening of the adsorption energy of the reactive intermediates caused by the Cu dopant leading to reduced strength in surface bonds as extensively elaborated in previous studies[50–52]. This could be corroborated by the reduced performance of BSCFZ5 despite the expansion in its lattice volume. The reduced electrocatalytic performance of BSCFZ5 however, could be attributed to the strengthening of the adsorption energy of the constitutive reactive intermediates thereby increasing the strength of the surface bonds in the perovskite structure[50]. [50]. Also, the pathway for oxygen diffusion is increased causing a reduction in the catalytic ORR of the parent BSCF material. Further insights into the electroactivity of the materials were investigated by estimating the activation energies

for each of the cathode materials using the Arrhenius plots generated from the ASR values of the respective cathode materials in **Figure 5c**. BSCFC5 was observed to have the least activation energy of 1.110 eV confirming the superiority of its electrocatalytic performance to BSCF. **Table S5** illustrates the comparison of the ASRs of various non-composite single-phase cathode materials that were derived from the traditional BSCF.

Since BSCFC5 demonstrated a better ASR relative to BSCF, and BSCFZ5 the improved ORR can be further expatiated by observing the effects of oxygen partial pressure (PO_2) on the area-specific resistance at different temperatures**. Figure 5(e-f)** illustrates the variation in polarization resistances relative to changes in oxygen partial pressure. The relation $R_p \propto (PO_2)^{-n}$ can be used to express the relationship between polarization resistance R_p and oxygen partial pressure (PO_2). The value n represents the rate-limiting step of oxygen reduction reaction as confirmed in previous studies [53–55]. This n exponent value has different connotations regarding the rate-limiting step for ORR depending on its value. When n = 0, 0.25, 0.375, 0.5, and 1, it means the rate-limiting step for ORR is due to ionic oxygen transfer from the triple-phase boundary to the electrolyte, charge transfer process on the electrode, charge transfer process at the triple-phase boundary, surface oxygen adsorptive dissociation and molecular oxygen adsorption and diffusion at the electrode surface, respectively [56]. It can be observed from **Figure 5** (**e-f)** that the polarization resistance decreases with an increasing oxygen partial pressure. From **Figure 5e,** the rate-limiting steps for oxygen reduction reaction of the cathode materials at 600 ℃ can be translated to be the charge transfer process on the electrode surface for BSCF and BSCFC5 while a charge transfer process at the triple-phase boundary is the rate-limiting step of ORR for BSCFZ5. However, the rate-limiting steps of ORR for BSCFC5 at 500 ℃ in **Figure 5f** are

predominantly molecular oxygen gas diffusion and partly surface exchange at the electrode surface.

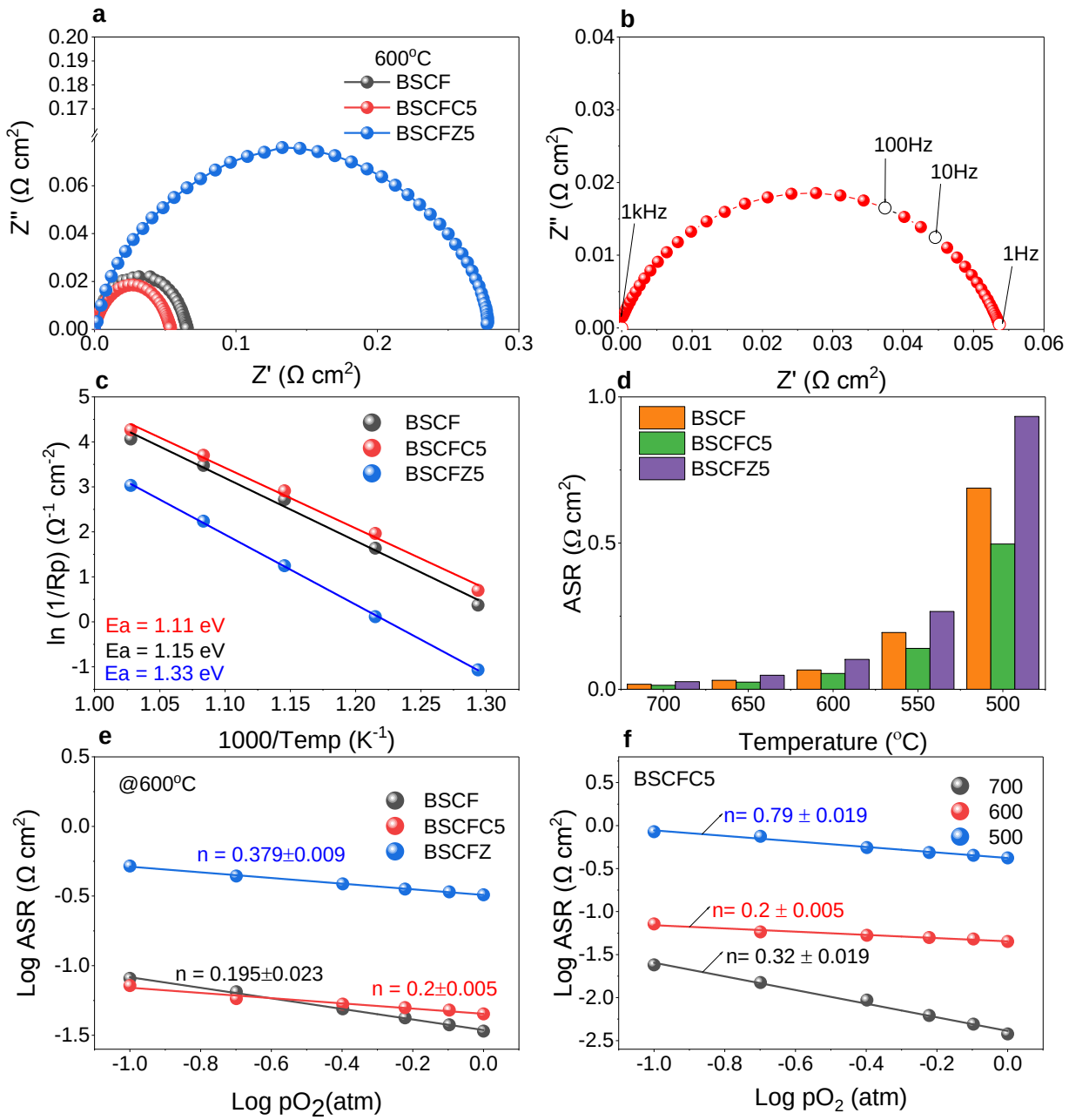

Figure 5: (a) Electrochemical impedance spectra for symmetric cells of BSCF, BSCFC5, and BSCFZ5 at 600 ℃ and (b) Impedance spectrum for the symmetric cell of BSCFC5 showing the frequencies for the charge transfer process and oxygen adsorptive-dissociation (c) Arrhenius plots of area-specific resistance values for BSCF, BSCFC5, and BSCFZ5 showing their various activation energies (d) The comparison of ASR of all the materials at different temperatures. The

variation in area-specific resistances with respect to changes in oxygen partial pressures for (e) BSCF, BSCFC5, and BSCFZ5 at 600 ℃ and (f) BSCFC5 at 500 ℃, 600 ℃, and 700 ℃.

To further gain insight into the complex ORR mechanism of BSCFC5 at different operation temperatures, distribution of relaxation time (DRT) analysis was conducted using the DRT tools package developed by Ciucci's lab[57]. From **Figure 6**, the plots can be segmented into three parts designated as P1, P2, and P3. The low-frequency region denoted as P3 (with frequency value $\leq 10^1$ Hz) corresponds to oxygen gas diffusion while P2 corresponds to surface exchange and ion diffusion between the electrode and electrolyte and P1(with frequency value $\geq 10^3$ Hz) denotes the charge transfer process at the interfaces as earlier discussed above[58–62]. Hence, the predominant rate-limiting step for ORR at $600 - 700$ ℃ in BSCFC5 is the charge transfer process on the electrode, and at the triple-phase boundary as illustrated in **Figure 6**. It can also be observed that generally, the rate-limiting process for ORR in region P2 decreases with increasing pO_2 for BSCFC5 at 600 ℃ while the rate-limiting process at region P1 at the same temperature were all fairly the same.

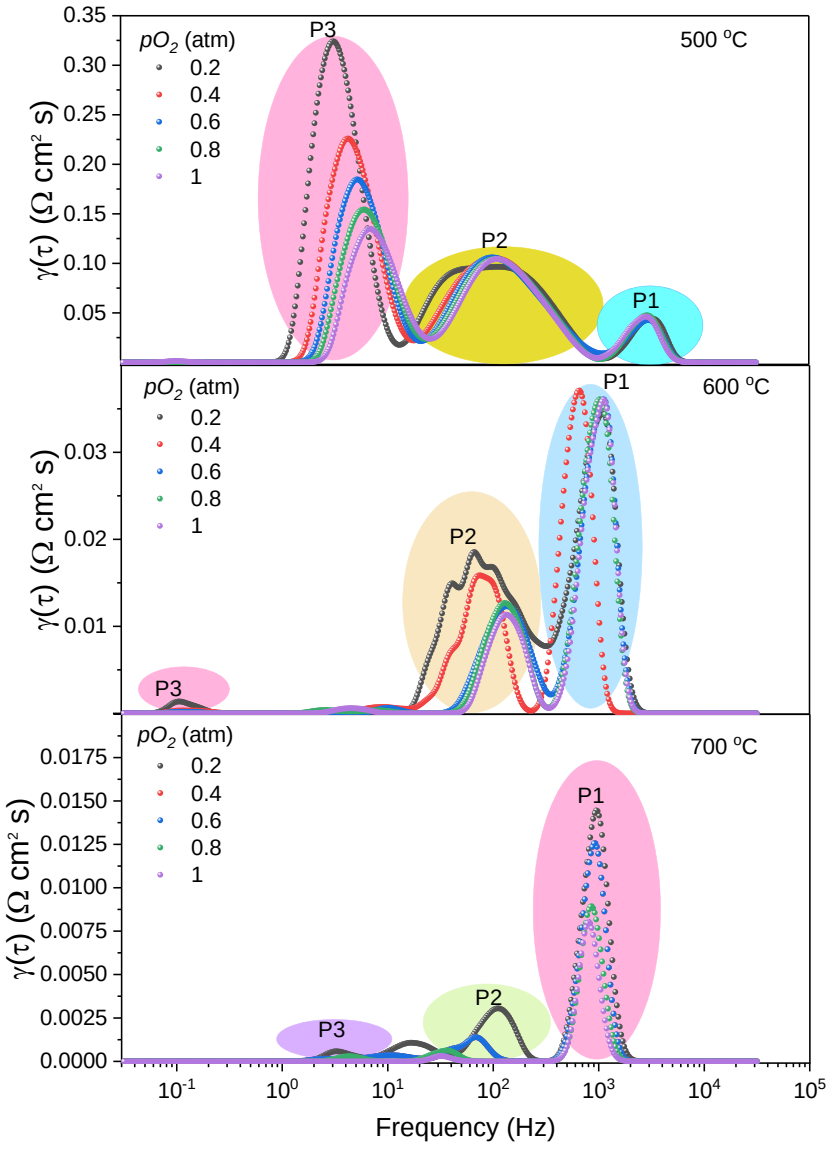

Figure 6: Distribution of relaxation time for the partial oxygen pressures of BSCFC5 air electrode material from 500-700 ℃.

The electrochemical performance of the materials can be further evaluated by taking I-V measurements of the anode-supported single cells as illustrated in **Figure 7**. The peak power densities of BSCF, BSCFC5, and BSCFZ5 are presented in **Figure 7(a-d)** while **Figure 7e**

summarizes the contrast between the PPDs of BSCF, BSCFC5, and BSCFZ5 at 500 ℃, 600 ℃, and 650 ℃, respectively. BSCFC5 demonstrated the best performance which implies that the substitution of Fe-TM in the B-site of the traditional BSCF with Cu triggered an increase in the PPD by 31% at 650 ℃ thereby confirming the better suitability of this material as cathode for intermediate temperature operating solid oxide fuel cells. The improved PPD of the BSCFC5 single cell could be attributed to the lattice contraction of the material as earlier explained thereby promoting efficient oxygen diffusion in the material with a shorter oxygen diffusion pathway and an increased O_{ads}/O_{lat} ratio of BSCFC5 from the XPS analysis. Also, **Figure 4** confirms that the atomic percentage is high thereby justifying the improved performance of BSCFC5. On the other hand, similar justification can be associated with the poorer performance of BSCFZ5 in the sense that the lattice volume expanded with a longer oxygen diffusion pathway and the O_{ads}/O_{lat} ratio significantly reduced thereby corroborating the reduced ORR of BSCFZ5. Notwithstanding, the observed reduced open-circuit voltage (OCV) of BSCF in **Figure 7a** could be attributed to the partial leakage of the supplied fuel during the testing. Nevertheless, the OCV values were all approximately $\sim 0.8\,V$ with the least being 0.77 V. As for the other cells, the OCV values tend to decrease with increasing temperature from 600 ℃ because the electrolyte material is ceria-based so it gets partially short-circuited at temperatures above 600 ℃ causing a reduction and hence, variation in the cell OCV values [63]. More specifically, the density and electrical conductivity of the electrolyte determines a cell OCV. Under reducing conditions, Ce^{4+} will be partially reduced to Ce^{3+} thereby enhancing the electronic conductivity of the cell. Likewise, as the temperature increases the electrical conductivity will increase causing a corresponding decrease in the cell OCV, usually at temperatures above 600 ℃.

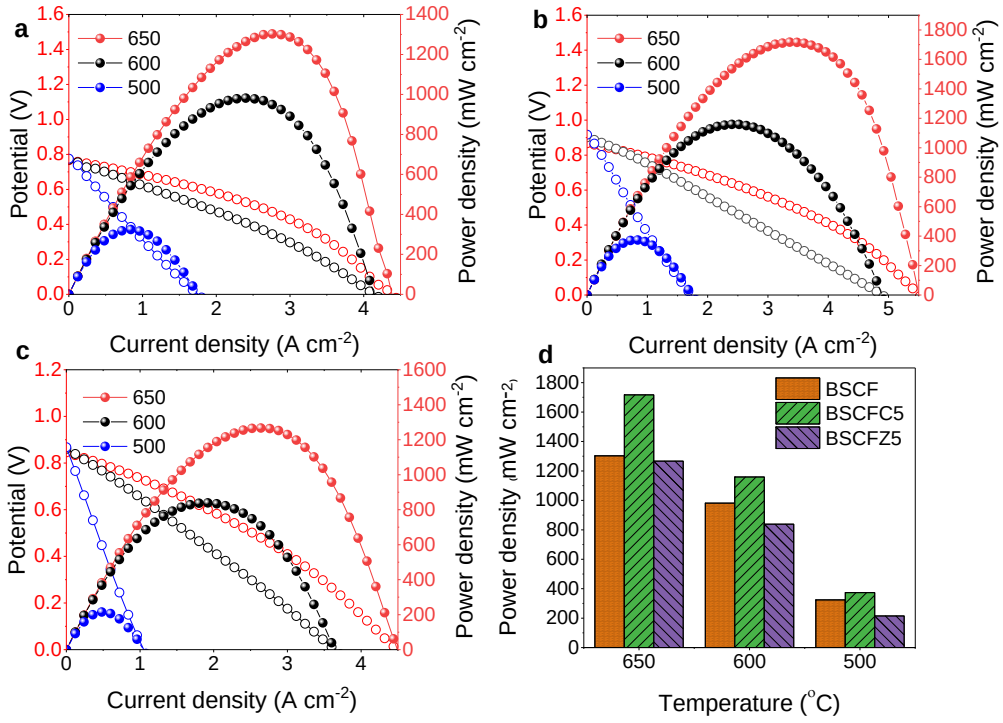

Figure 7: The *I-V-P* curves of single cells from 500 ℃ to 650 ℃ for (a) NiO-SDC | SDC | BSCF (b) NiO-SDC | SDC | BSCFC5 (c) NiO-SDC | SDC | BSCFZ5 and (d) Visual illustrative comparison of the PPDs for the materials at different temperatures.

Durability is another important and basic assessment requirement of cathode materials for SOFC practical applications. The material with superior performance (BSCFC5) was selected for this test. An approximately 185 hours stability test was carried out on the symmetric cell based on BSCFC5 relative to the undoped BSCF material using pure air at a flow rate of 100 mL min^{-1} as illustrated in **Figure 8**. The material exhibited reasonable stability in pure air during the test which suggests that the material has good performance stability.

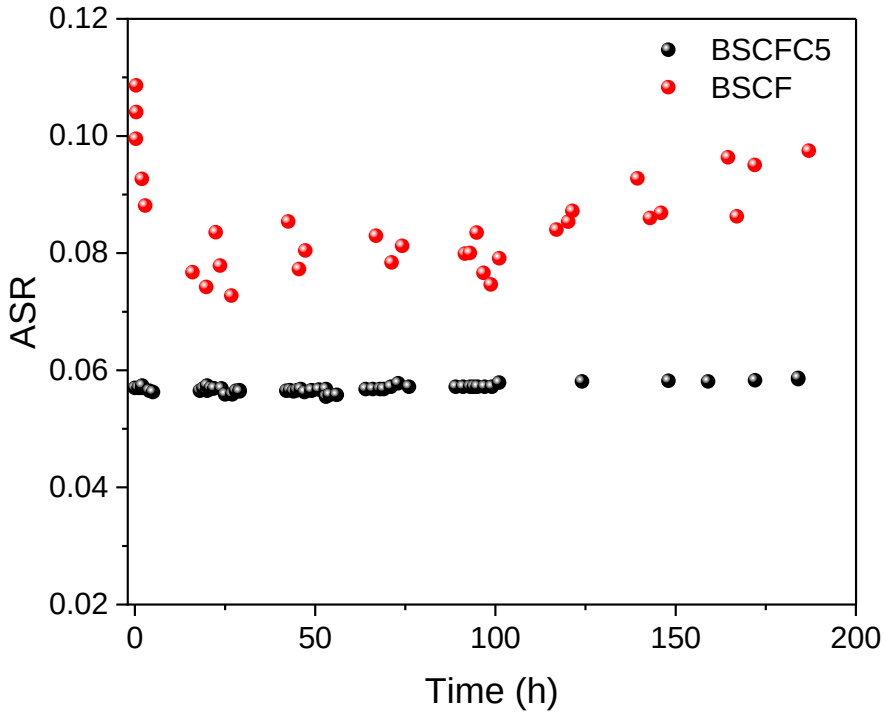

Figure 8: Stability of the ASR of BSCFC5 and BSCF after 180 hrs. at 600 ℃.

Thereafter, a CO_2 exposure test was also carried out on BSCF, BSCFC5, and BSCFZ5 powders to observe the degree of the degradation and insurgence of foreign phases in the crystal structures of the perovskite samples. The powders were exposed to 100 % CO_2 gas at the flow rate of 50 mL min^{-1} at 600 ^oC for 24 hrs in a tubular furnace. The resulting crystal structure of the materials is presented in **Figure S2** and the refinement in **Figure S3**. BSCFZ5 appeared to be more chemically stable in the CO_2 atmosphere even though they all reacted to the CO_2 atmosphere through the formation of $BaCO_3$ phases. The degree of degradation of the exposed BSCF sample, however, is more severe as seen in **Table S1** where the lattice volume increased by 0.67 % while those of BSCFC5 and BSCFZ5 increased by 0.36 % and 0.14 %, respectively. Hence, the stabilities of BSCFC5 and BSCFZ5 both improved and the better stability of BSCFZ5 is rational because there has been a trade-off between its performance and stability. Nevertheless,

BSCFC5 can be confirmed to be the most optimal material with a simultaneous improvement in its performance and chemical stability thereby promoting it as a superior alternative for intermediate temperature solid oxide fuel cell applications. Moreover, it has been suggested in previous studies that adsorbed oxygen can be linked with CO_2 and functional groups containing oxygen (i.e., OH^-, CO_3^{2-}, O^{2-}, and O^-)[64,65]. It is worthy of note that the adsorbed oxygen content of BSCF increased by 2.36% with Cu substitution in its B-site. Also, the mechanism of the CO_2 reduction reaction has been established to be associated with the valency of oxygen in air electrode materials[66]. Hence the adsorption and reduction reaction of CO_2 in BSCF is improved with Cu-doping.

To further buttress the effect of the CO_2 atmosphere in the samples, the ASRs of their symmetric cells were observed at different intervals with the injection and ejection of 10 vol% CO_2 as shown in **Figure 9a.**

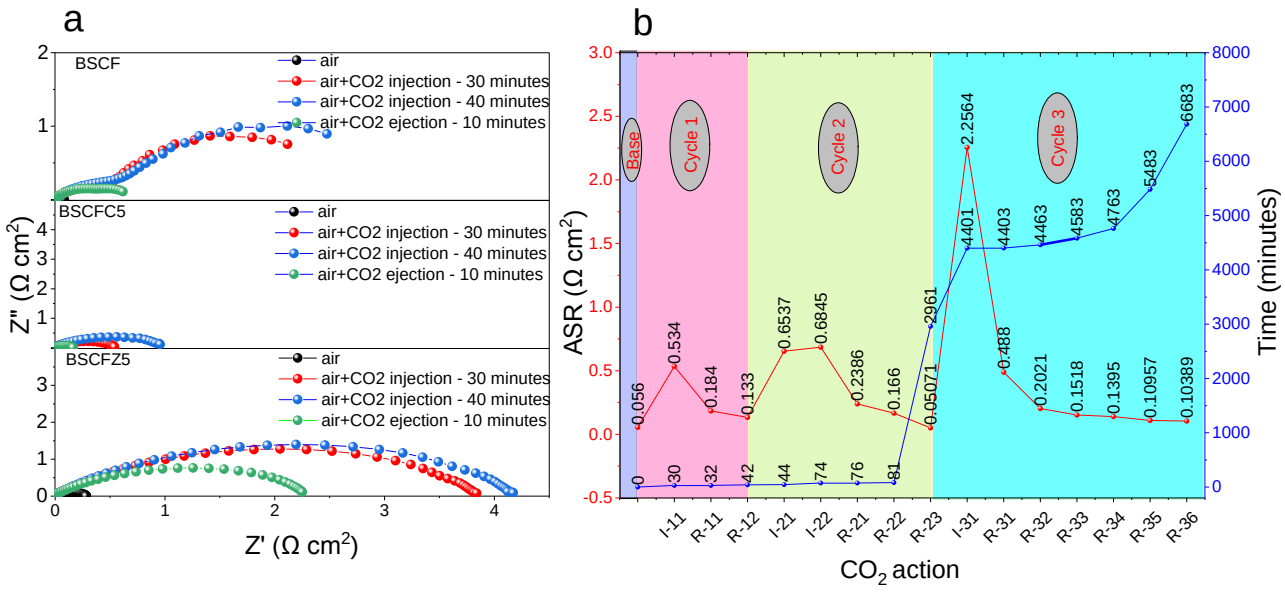

Figure 9: (a) Impedance spectra for BSCF, BSCFC5, and BSCFZ5 at 600 ℃ under pure air and injection and ejection of 10 % CO_2. (b) Cyclic Injection and ejection of 10 vol% CO_2 in BSCFC5 at 600 ℃ and different times, where I = Injection and R = Recovery.

The ASRs of BSCF, BSCFC5 and BSCFZ5 were first tested in pure air followed by the injection of 10 vol% CO_2 into the cell for 30 minutes which was later extended to 40 minutes. The performances of all the materials degraded with time when CO_2 was infused into the cells and BSCF appears to be more affected by the CO_2 infusion relative to BSCFZ5 and BSCFC5. This confirms the relative superiority of BSCFC5 and BSCFZ5 to CO_2. After 10 minutes of the ejection of the 10 vol% CO_2 from all the samples, their performances improved. Nonetheless, BSCFC5 can be validated to be the optimal material based on its overall performance during the ASR test in a CO_2-rich atmosphere. To get more insights into BSCFC5 material response to CO_2, a cyclic test was then carried out in which CO_2 was injected and ejected at 600 ℃ and different intervals as shown in **Figure 9b**. At first, in the base section, pure air was used for the test to get an ASR of 0.056 Ω cm^2. Secondly, 10 vol% CO_2 was injected into the cell for 30 minutes causing the ASR to increase to 0.534 Ω cm^2 which was then followed by a recovery (ejection of the CO_2) for 2 and 30 minutes. This caused the ASR to reduce to 0.184 Ω cm^2 and 0.133 Ω cm^2, respectively. The 10 vol% CO_2 was passed into the cell for 2 minutes and then another 30 minutes, again the ASR increased to 0.685 Ω cm^2. The recovery process was initiated which lasted for 2887 minutes to get an ASR as low as 0.051 Ω cm^2. Again, 10 vol% CO_2 was injected for 1440 minutes. The ASR increased to 2.564 Ω cm^2 and after an ejection process that lasted for 2282 minutes, the ASR reduced to 0.104 Ω cm^2. Hence, after cyclic exposure of CO_2 to BSCFC5 for a total of 6683 minutes, the performance of the material only reduced by 46% from 0.056 Ω cm^2 to 0.104 Ω cm^2 at 600 ℃. This promotes this material as an excellent substitute for BSCF in fuel cell and electrolysis cell applications.

Conclusion

In conclusion, we have systematically engineered the lattice expansion and contraction of BSCF functional material by partially substituting the Fe-B-site cation with the TMs, Zn, and Cu, respectively. We were able to show that lattice engineering is a significant descriptor to evince the variability in the catalytic ORR and CO_2 tolerance of BSCF functional material. Enhanced catalytic ORR and CO_2 tolerance was also correlated with lattice contraction due to the shortened pathway for oxygen mobility in the lattice of BSCF and the weakened adsorption energy of the constitutive reactive intermediates. Cu-TM instigated a contraction while Zn-TM instigated an expansion in the lattice of BSCF. The BSCFC5 cathode where lattice contraction occurred, exhibits the best performance with an ASR of 0.0247 Ω cm^2 and a high peak power density (PPD) of 1715 mW cm^{-2} at 650 ℃ for the symmetrical and single cells, respectively. The material also displayed enhanced tolerance to CO_2 infusion with a satisfactory display of recoverability when switched intermittently between pure air and 10 vol% CO_2 infusions for 100 hours. Our findings lead us to the conclusion that Cu-TM doped BSCF, (BSCFC5) is a better substitute for BSCF material for SOFC applications.

References

[1] Hall JL. Cell components. Phytochemistry 1987;26:1235–6. https://doi.org/10.1016/s0031-9422(00)82398-5.

[2] Carrette L, Friedrich KA, Stimming U. Fuel Cells - Fundamentals and Applications. Fuel Cells 2001;1:5–39. https://doi.org/10.1002/1615-6854(200105)1:1<5::aid-fuce5>3.0.co;2-g.

[3] Bello IT, Zhai S, He Q, Xu Q, Ni M. ScienceDirect Scientometric review of

advancements in the development of high-performance cathode for low and intermediate temperature solid oxide fuel cells : Three decades in retrospect. Int J Hydrogen Energy 2021. https://doi.org/10.1016/j.ijhydene.2021.05.134.

[4] Bello IT, Chen B. Materials development and prospective for protonic ceramic fuel cells 2021:1–29. https://doi.org/10.1002/er.7371.

[5] Yang G, Su C, Shi H, Zhu Y, Song Y, Zhou W, et al. Toward reducing the operation temperature of solid oxide fuel cells: Our past 15 years of efforts in cathode development. Energy and Fuels 2020;34:15169–94. https://doi.org/10.1021/acs.energyfuels.0c01887.

[6] Sasaki K, Wurth J - P., Gschwend R, Gödickemeier M, Gauckler LJ. Microstructure-Property Relations of Solid Oxide Fuel Cell Cathodes and Current Collectors: Cathodic Polarization and Ohmic Resistance. J Electrochem Soc 1996;143:530–43. https://doi.org/10.1149/1.1836476.

[7] Xu Q, Guo Z, Xia L, He Q, Li Z, Temitope I, et al. A comprehensive review of solid oxide fuel cells operating on various promising alternative fuels. Energy Convers Manag 2022;253:115175. https://doi.org/10.1016/j.enconman.2021.115175.

[8] Bello IT, Zhai S, He Q, Xu Q, Ni M. Scientometric review of advancements in the development of high-performance cathode for low and intermediate temperature solid oxide fuel cells: Three decades in retrospect. Int J Hydrogen Energy 2021;46:26518–36. https://doi.org/10.1016/j.ijhydene.2021.05.134.

[9] Liu T, Zhao Y, Zhang X, Zhang H, Jiang G, Zhao W, et al. Robust redox-reversible perovskite type steam electrolyser electrode decorated with: In situ exsolved metallic nanoparticles. J Mater Chem A 2020;8:582–91. https://doi.org/10.1039/c9ta06309a.

[10] Porras-Vazquez JM, Slater PR. Synthesis of oxyanion-doped barium strontium cobalt ferrites: Stabilization of the cubic perovskite and enhancement in conductivity. J Power Sources 2012;209:180–3. https://doi.org/10.1016/j.jpowsour.2012.02.105.

[11] Zeng Q, Zhang X, Wang W, Zhang D, Jiang Y, Zhou X, et al. A Zn-doped Ba0.5Sr0.5Co0.8Fe0.2o3-δ perovskite cathode with enhanced ORR catalytic activity for SOFCs. Catalysts 2020;10:1–12. https://doi.org/10.3390/catal10020235.

[12] Huang Y, Ding J, Xia Y, Miao L, Li K, Zhang Q, et al. Ba0.5Sr0.5Co0.8-xFe0.2NbxO3-δ (x≤0.1) as cathode materials for intermediate temperature solid oxide fuel cells with an electron-blocking interlayer. Ceram Int 2020;46:10215–23. https://doi.org/10.1016/j.ceramint.2020.01.013.

[13] Duan C, Hook D, Chen Y, Tong J, O'Hayre R. Zr and Y co-doped perovskite as a stable, high performance cathode for solid oxide fuel cells operating below 500°C. Energy Environ Sci 2017;10:176–82. https://doi.org/10.1039/c6ee01915c.

[14] Sun YR, Zhang X, Wang LG, Liu ZK, Kang N, Zhou N, et al. Lattice contraction tailoring in perovskite oxides towards improvement of oxygen electrode catalytic activity. Chem Eng J 2021;421:129698. https://doi.org/10.1016/j.cej.2021.129698.

[15] Shao Z, Yang W, Cong Y, Dong H, Tong J, Xiong G. Investigation of the permeation behavior and stability of a Ba0.5Sr0.5Co0.8Fe0.2O(3-δ) oxygen membrane. J Memb Sci 2000;172:177–88. https://doi.org/10.1016/S0376-7388(00)00337-9.

[16] Shao Z, Haile SM. A high-performance cathode for the next generation of solid-oxide fuel cells. Mater Sustain Energy A Collect Peer-Reviewed Res Rev Artic from Nat Publ Gr 2004;3:255–8. https://doi.org/10.1142/9789814317665_0036.

[17] Kim J, Choi S, Jun A, Jeong HY, Shin J, Kim G. Chemically stable perovskites as cathode materials for solid oxide fuel cells: La-Doped Ba0.5Sr0.5Co0.8Fe 0.2O3-δ. ChemSusChem 2014;7:1669–75. https://doi.org/10.1002/cssc.201301401.

[18] Wei B, Lü Z, Huang X, Li S, Ai G, Liu Z, et al. Electrochemical characteristics of Ba0.5Sr0.5Co0.8Fe0.2O3-δ-Sm0.2Ce0.8O1.9 composite materials for low-temperature solid oxide fuel cell cathodes. Mater Lett 2006;60:3642–6. https://doi.org/10.1016/j.matlet.2006.03.075.

[19] Li S, Lü Z, Wei B, Huang X, Miao J, Liu Z, et al. Performances of Ba0.5Sr0.5Co0.6Fe0.4O3-δ-Ce0.8Sm0.2O1.9 composite cathode materials for IT-SOFC. J Alloys Compd 2008;448:116–21. https://doi.org/10.1016/j.jallcom.2006.10.032.

[20] Kao WX, Lee MC, Lin TN, Wang CH, Chang YC. Fabrication and characterization of a Ba0.5Sr0.5Co0.8Fe0.2O3- δ-Gadolinia-doped ceria cathode for an anode-supported solid-oxide fuel cell. J Power Sources 2010;195:2220–3. https://doi.org/10.1016/j.jpowsour.2009.10.057.

[21] Li L, Yang H, Gao Z, Zhang Y, Dong F, Yang G, et al. Nickel-substituted Ba0.5Sr0.5Co0.8Fe0.2O3-δ: a highly active perovskite oxygen electrode for reduced-temperature solid oxide fuel cells. J Mater Chem A 2019;7:12343–9. https://doi.org/10.1039/c9ta02548k.

[22] Xu X, Su C, Shao Z. Fundamental Understanding and Application of Ba 0.5 Sr 0.5 Co 0.8 Fe 0.2 O 3−δ Perovskite in Energy Storage and Conversion: Past, Present, and Future . Energy & Fuels 2021;35:13585–609. https://doi.org/10.1021/acs.energyfuels.1c02111.

[23] Su C, Wang W, Shao Z. Cation-De fi cient Perovskites for Clean Energy Conversion

2021. https://doi.org/10.1021/accountsmr.1c00036.

[24] Escudero-Escribano M, Malacrida P, Hansen HM, Vej-Hansen U, Velazquez-Palenzuela A, Tripkovic V, et al. Dering That Can Enable the Engineering of Material Properties Through Spontaneous Ordering of Nanoparticles. Science (80-) 2016;352:73–6.

[25] Cai J, Song Y, Zang Y, Niu S, Wu Y, Xie Y, et al. N-induced lattice contraction generally boosts the hydrogen evolution catalysis of P-rich metal phosphides. Sci Adv 2020;6:1–9. https://doi.org/10.1126/sciadv.aaw8113.

[26] Liu J, Li Q, Sun L, Huo L, Zhao H, Jean-marc B. Tuning the high temperature properties of PrSrCoO 4 cathode with Cu 2 þ dopant for intermediate temperature solid oxide fuel cells 2020;159:486–93. https://doi.org/10.1016/j.renene.2020.06.032.

[27] Aguadero A, Alonso JA, Escudero MJ, Daza L. Evaluation of the La2Ni1−xCuxO4+δ system as SOFC cathode material with 8YSZ and LSGM as electrolytes. Solid State Ionics 2008;179:393–400. https://doi.org/https://doi.org/10.1016/j.ssi.2008.01.099.

[28] NOMURA T, NISHIMOTO S, KAMESHIMA Y, MIYAKE M. Electrode properties of doped Pr_2NiO_4-based oxide cathode for intermediate-temperature SOFCs. J Ceram Soc Japan 2012;120:534–8. https://doi.org/10.2109/jcersj2.120.534.

[29] Xie J, Ju Y-W, Matsuka M, Ida S, Ishihara T. Synergy effects of Pr1.91Ni0.71Cu0.24Ga0.05O4 and Ba0.5La0.5CoO3 composite on cathodic activity for intermediate temperature solid oxide fuel cells. J Power Sources 2013;228:229–36. https://doi.org/https://doi.org/10.1016/j.jpowsour.2012.11.089.

[30] Fu YP, Subardi A, Hsieh MY, Chang WK. Electrochemical Properties of

La0.5Sr0.5Co0.8M0.2O3-δ (M=Mn, Fe, Ni, Cu) Perovskite Cathodes for IT-SOFCs. J Am Ceram Soc 2016;99:1345–52. https://doi.org/10.1111/jace.14127.

[31] Wan Yusoff WNA, Somalu MR, Baharuddin NA, Muchtar A, Wei LJ. Enhanced performance of lithiated cathode materials of LiCo0.6X0.4O2 (X = Mn, Sr, Zn) for proton-conducting solid oxide fuel cell applications. Int J Energy Res 2020;44:11783–93. https://doi.org/10.1002/er.5819.

[32] Park J, Zou J, Yoon H, Kim G, Chung JS. Electrochemical behavior of Ba0.5Sr0.5Co 0.2-xZnxFe0.8O3-δ (x = 0-0.2) perovskite oxides for the cathode of solid oxide fuel cells. Int J Hydrogen Energy 2011;36:6184–93. https://doi.org/10.1016/j.ijhydene.2011.01.142.

[33] Li K, Xue D. Estimation of electronegativity values of elements in different valence states. J Phys Chem A 2006;110:11332–7. https://doi.org/10.1021/jp062886k.

[34] Slater JC. Atomic radii in crystals. J Chem Phys 1964;41:3199–204. https://doi.org/10.1063/1.1725697.

[35] Gagné OC, Hawthorne FC. Empirical Lewis acid strengths for 135 cations bonded to oxygen. Acta Crystallogr Sect B Struct Sci Cryst Eng Mater 2017;73:956–61. https://doi.org/10.1107/S2052520617010988.

[36] Liu D, Dou Y, Xia T, Li Q, Sun L, Huo L, et al. B-site La, Ce, and Pr-doped Ba0.5Sr0.5Co0.7Fe0.3O3-δ perovskite cathodes for intermediate-temperature solid oxide fuel cells: Effectively promoted oxygen reduction activity and operating stability. J Power Sources 2021;494:229778. https://doi.org/10.1016/j.jpowsour.2021.229778.

[37] Wang X, Dou Y, Xie Y, Wang J, Xia T, Huo L, et al. A-Site Cation-Ordering Layered

Perovskite EuBa0.5Sr0.5Co2-xFexO5+δas Highly Active and Durable Electrocatalysts for Oxygen Evolution Reaction. ACS Omega 2020;5:12501–15. https://doi.org/10.1021/acsomega.0c01383.

[38] Jin F, Liu X, Chu X, Shen Y, Li J. Effect of nonequivalent substitution of Pr3+/4+ with Ca2+ in PrBaCoFeO5+δ as cathodes for IT-SOFC. J Mater Sci 2021;56:1147–61. https://doi.org/10.1007/s10853-020-05375-y.

[39] Gao L, Zhu M, Li Q, Sun L, Zhao H, Grenier J-C. Electrode properties of Cu-doped Bi0.5Sr0.5FeO3−δcobalt-free perovskite as cathode for intermediate-temperature solid oxide fuel cells. J Alloys Compd 2017;700:29–36. https://doi.org/10.1016/j.jallcom.2017.01.026.

[40] Shen Y, Zhao H, Świerczek K, Du Z, Xie Z. Lattice structure, sintering behavior and electrochemical performance of La1.7Ca0.3Ni1−xCuO4+Δ as cathode material for intermediate-temperature solid oxide fuel cell. J Power Sources 2013;240:759–65. https://doi.org/10.1016/j.jpowsour.2013.05.025.

[41] Zhang W, Zhang L, Guan K, Zhang X, Meng J, Wang H, et al. Effective promotion of oxygen reduction activity by rare earth doping in simple perovskite cathodes for intermediate-temperature solid oxide fuel cells. J Power Sources 2020;446:227360. https://doi.org/10.1016/j.jpowsour.2019.227360.

[42] Xu X, Wang H, Fronzi M, Wang X, Bi L, Traversa E. Tailoring cations in a perovskite cathode for proton-conducting solid oxide fuel cells with high performance. J Mater Chem A 2019;7:20624–32. https://doi.org/10.1039/c9ta05300j.

[43] Sun L-P, Li H, Li Q, Huo L-H, Zhao H, Bassat J-M, et al. Evaluation of La2-xNiMnO6-Δ

as cathode for intermediate temperature solid oxide fuel cells. J Power Sources 2018;392:8–14. https://doi.org/10.1016/j.jpowsour.2018.04.083.

[44] Gao L, Zhu M, Li Q, Sun L, Zhao H, Grenier JC. Electrode properties of Cu-doped Bi0.5Sr0.5FeO3−δcobalt-free perovskite as cathode for intermediate-temperature solid oxide fuel cells. J Alloys Compd 2017;700:29–36. https://doi.org/10.1016/j.jallcom.2017.01.026.

[45] Wang M, Jiang L, Kim EJ, Hahn SH. Electronic structure and optical properties of Zn(OH)2: LDA+U calculations and intense yellow luminescence. RSC Adv 2015;5:87496–503. https://doi.org/10.1039/c5ra17024a.

[46] Brown ID, Skowron A. Electronegativity and Lewis Acid Strength. J Am Chem Soc 1990;112:3401–3. https://doi.org/10.1021/ja00165a023.

[47] Yáng Z, Harvey AS, Infortuna A, Schoonman J, Gauckler LJ. Electrical conductivity and defect chemistry of Ba xSr 1-xCo yFe 1-yO 3-deltaperovskites. J Solid State Electrochem 2011;15:277–84. https://doi.org/10.1007/s10008-010-1208-4.

[48] Lin Y, Ran R, Zheng Y, Shao Z, Jin W, Xu N, et al. Evaluation of Ba0.5Sr0.5Co0.8Fe0.2O3−δ as a potential cathode for an anode-supported proton-conducting solid-oxide fuel cell. J Power Sources 2008;180:15–22. https://doi.org/https://doi.org/10.1016/j.jpowsour.2008.02.044.

[49] Adler SB. Limitations of charge-transfer models for mixed-conducting oxygen electrodes. Solid State Ionics 2000;135:603–12. https://doi.org/10.1016/S0167-2738(00)00423-9.

[50] Strasser P, Koh S, Anniyev T, Greeley J, More K, Yu C, et al. core – shell fuel cell

catalysts 2010;2:454–60. https://doi.org/10.1038/nchem.623.

[51] Nilsson A, Pettersson LGM, Hammer B, Bligaard T, Christensen CH, Nørskov JK. The electronic structure effect in heterogeneous catalysis 2005;100:111–4. https://doi.org/10.1007/s10562-004-3434-9.

[52] Nilsson A, Pettersson LGM, Norskov JK. Chemical Bonding at Surfaces and Interfaces. 1st ed. Elsevier; 2007.

[53] Almar L, Störmer H, Meffert M, Szász J, Wankmüller F, Gerthsen D, et al. Improved Phase Stability and CO2 Poisoning Robustness of Y-Doped Ba0.5Sr0.5Co0.8Fe0.2O3-δ SOFC Cathodes at Intermediate Temperatures. ACS Appl Energy Mater 2018;1:1316–27. https://doi.org/10.1021/acsaem.8b00028.

[54] Fabbri E, Bi L, Pergolesi D, Traversa E. High-performance composite cathodes with tailored mixed conductivity for intermediate temperature solid oxide fuel cells using proton conducting electrolytes. Energy Environ Sci 2011;4:4984–93. https://doi.org/10.1039/c1ee02361f.

[55] Serra JM, Vert VB. Compositional IMPROVEMENT of Ln0.435Ba0.145Sr 0.4Fe0.8Co0.2O3-δIT-SOFC cathodes performance by multiple lanthanide substitution. J Electrochem Soc 2010;157. https://doi.org/10.1149/1.3465646.

[56] Wang J, Saccoccio M, Chen D, Gao Y, Chen C, Ciucci F. The effect of A-site and B-site substitution on BaFeO 3 À d : An investigation as a cathode material for intermediate-temperature solid oxide fuel cells. J Power Sources 2015;297:511–8. https://doi.org/10.1016/j.jpowsour.2015.08.016.

[57] Wan TH, Saccoccio M, Chen C, Ciucci F. Influence of the Discretization Methods on the Distribution of Relaxation Times Deconvolution: Implementing Radial Basis Functions with DRTtools. Electrochim Acta 2015;184:483–99. https://doi.org/10.1016/j.electacta.2015.09.097.

[58] Plekhanov SS, Kuzmin A V., Tropin ES, Korolev DA, Ananyev M V. New mixed ionic and electronic conductors based on LaScO3: Protonic ceramic fuel cells electrodes. J Power Sources 2020;449:227476. https://doi.org/10.1016/j.jpowsour.2019.227476.

[59] Song KE, Woo SH, Baek SW, Kang H, Choi WS, Park JY, et al. SmBa1-xCaxCo2O5+d Layered Perovskite Cathodes for Intermediate Temperature-operating Solid Oxide Fuel Cells. Front Chem 2021;8. https://doi.org/10.3389/fchem.2020.628813.

[60] Sumi H, Ohshiro T, Nakayama M, Suzuki T, Fujishiro Y. Prevention of Reaction between (Ba,Sr)(Co,Fe)O3 Cathodes and Yttria-stabilized Zirconica Electrolytes for Intermediate-temperature Solid Oxide Fuel Cells. Electrochim Acta 2015;184:403–9. https://doi.org/10.1016/j.electacta.2015.10.092.

[61] Hashim SS, Liang F, Zhou W, Sunarso J. Cobalt-Free Perovskite Cathodes for Solid Oxide Fuel Cells. ChemElectroChem 2019;6:3549–69. https://doi.org/10.1002/celc.201900391.

[62] Chen Y, Yoo S, Choi Y, Kim JH, Ding Y, Pei K, et al. A highly active, CO2-tolerant electrode for the oxygen reduction reaction† 2018:2458–66. https://doi.org/10.1039/c8ee01140k.

[63] Liu M, Ding D, Bai Y, He T, Liu M. An Efficient SOFC Based on Samaria-Doped Ceria (SDC) Electrolyte. J Electrochem Soc 2012;159:B661–5.

https://doi.org/10.1149/2.032206jes.

[64] Xu C, Zhen S, Ren R, Chen H, Song W, Wang Z, et al. Cu-Doped Sr2Fe1.5Mo0.5O6−δ as a highly active cathode for solid oxide electrolytic cells 2019:8009–12. https://doi.org/10.1039/c9cc03455b.

[65] Zhang Z, Zhu Y, Zhong Y, Zhou W, Shao Z. Anion Doping: A New Strategy for Developing High-Performance Perovskite-Type Cathode Materials of Solid Oxide Fuel Cells. Adv Energy Mater 2017;7. https://doi.org/10.1002/aenm.201700242.

[66] Environ E, Zhi M, Zhou G, Hong Z, Wang J, Gemmen R, et al. Energy & Environmental Science 2011:139–44. https://doi.org/10.1039/c0ee00300j.